Electronic Supplementary Material (ESI) for Journal of Materials Chemistry C.

Supporting Information

High Performance Non-Doped Green Organic Light Emitting Diode via Delayed Fluorescence

Bahadur Sk,[a] *Vasudevan Thangaraji,*[b] *Nisha Yadav,*[a] *Gyana Prakash Nanda,*[a] *Sannibha Das,*[a] *Parthasarathy Gandeepan,**[c] *Eli Zysman-Colman,**[d] *and Pachaiyappan Rajamalli**[a]

[a] Materials Research Centre, Indian Institute of Science, Bangalore-560012, Karnataka, India

*E-mail: rajamalli@iisc.ac.in

[b] Department of Chemistry, National Tsing Hua University, Hsinchu 30013, Taiwan.

[c] Department of Chemistry, Indian Institute of Technology Tirupati, Tirupati, Andhra Pradesh 517506, India. E-mail: pgandeepan@iittp.ac.in

[d] Organic Semiconductor Centre, EaStCHEM School of Chemistry, University of St Andrews, St Andrews, United Kingdom. E-mail: eli.zysman-colman@st-andrews.ac.uk

Table of contents

General Information

The ^{1}H and ^{13}C NMR spectra were recorded using Varian mercury 400 spectrometer. The HRMS were measured on a MAT-95XL HRMS. UV-vis absorption spectra were recorded on a Hitachi U-3300 spectrophotometer. PL spectra and phosphorescent spectra were measured using Hitachi F-7000 spectrophotometer. The electrochemical properties were measured by 600s A CH Instruments. The decomposition temperature was determined by TGA using TG/DTA Seiko SSC-5200 instrument. The electrochemical properties were measured using CH Instruments 600A electrochemical analyzer. The oxidation measurements were measured using glassy carbon electrode as the working electrode, an Ag/Ag^{+} (0.01 M $AgNO_3$) as the reference electrode and Pt wire as the counter electrode, respectively in dichloromethane. The absolute PL quantum efficiency of the doped films were determined using an integrating sphere under N_2 atmosphere. Transient decay curves were measured using an Edinburgh Instruments F980 spectrofluorimeter. The Transient decay curves for prompt fluorescence were measured using time correlated single photon counting (TCSPC) while delayed fluorescence decays were measured using multi-channel scaling (MCS).

OLEDs Fabrication and Measurement

Organic materials used in device fabrication were usually purified by sublimation. Device were fabricated by vacuum deposition onto pre-coated ITO glass with sheet resistance of 25 Ω/square at a pressure lower than 10^{-6} Torr. Organic materials were deposited at the rate of 0.5~1.2 Å s^{-1}. LiF and Al were deposited at the rate of 0.1 Å s^{-1}, 3-10 Å s^{-1}, respectively. The rest of the procedures are similar to the reported method.[1]

Synthesis procedure

Synthesis of *N,N*-di-*p*-tolylanthracen-9-amine (TAA)

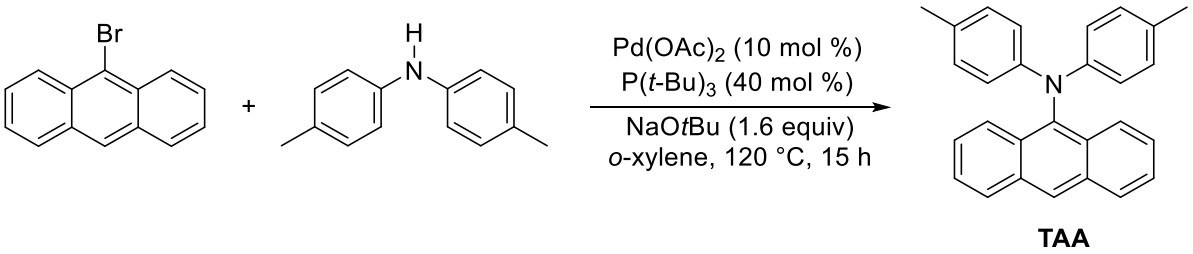

TAA

The reaction was performed following the reported procedure.[2] A mixture of 9-bromoanthracene (5.0 g, 19.5 mmol), $Pd(OAc)_2$ (43.0 mg, 0.19 mmol), tri-*tert*-butylphosphine (158.0 mg, 0.78 mmol), di-*p*-tolylamine (4.24 g, 21.6 mmol) and sodium *tert*-butoxide (3.10 g, 32 mmol) in dry *o*-xylene (40 mL) was placed in a sealed tube under a nitrogen atmosphere and was stirred at 120 ºC for 15 h. After cooling, water was added to the reaction mixture and the mixture was then extracted with ethyl acetate. The organic layer was dried over anhydrous $MgSO_4$ and evaporated under vacuum. The products were purified by silica gel column chromatography eluted with *n*-hexane. Yellow solid of **TAA** was obtained in 89% yield. The spectral data are in accordance with the previously published results.[2]

Synthesis of 10-bromo-*N,N*-di-*p*-tolylanthracen-9-amine (TAAB)[2]

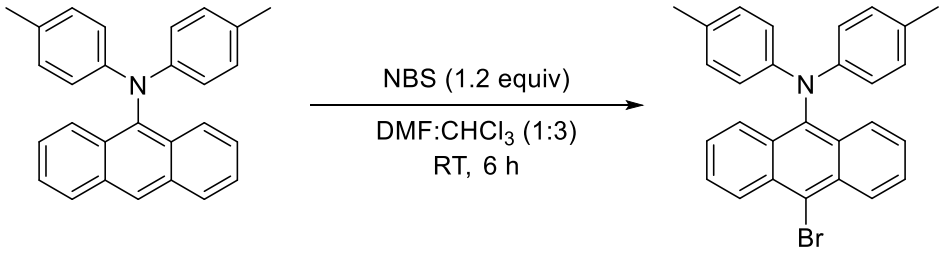

TAA **TAAB**

The reaction was performed following the reported procedure.[2] TAA (5.00 g, 134 mmol) and *N*-bromosuccinimide (NBS) (2.86 g, 161 mmol) were dissolved in DMF: $CHCl_3$ (1:3, 60 mL) and the solution was stirred at room temperature for 6 h. After completion of reaction, water was added to the reaction mixture and the mixture was extracted with dichloromethane. The organic layer was dried over anhydrous $MgSO_4$ and evaporated

under vacuum. The product was purified by silica gel column chromatography eluted with *n*-hexane. Red crystals of TAAB were obtained in 86% yield. The spectral data are in accordance with the previously published results.[2]

10-(4-Bromophenyl)-*N*,*N*-di-*p*-tolylanthracen-9-amine (TAAPB)

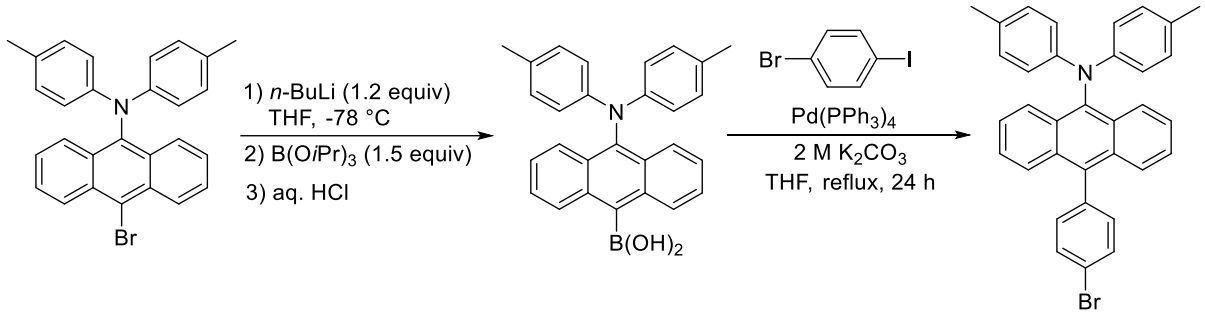

TAAB **TAABO** **TAAPB**

To a solution of TAAB (2.0 g, 4.4 mmol) in THF (75 mL) cooled to -78 °C under a nitrogen atmosphere was added dropwise *n*-BuLi (2.5 M solution in hexane, 2.6 mL, 5.3 mmol). The mixture was stirred for 1 h at -78 °C. Tri*iso*propyl borate (1.3 g, 6.6 mmol) was then added quickly via syringe. The reaction mixture was stirred for another 2 h before being allowed to warm to room temperature. Aqueous HCl (5%) was added to bring the pH to 5-6. The mixture was then extracted with dichloromethane. The organic phase was washed with water and dried with $MgSO_4$ and the solvents removed under reduced pressure. A yellow powder (TAABO) was obtained and was used as such in the next step. To a solution of TAABO (4 g, 9.6 mmol) and 4-bromo-iodobenzene (4 g, 14.3 mmol) in 10 ml of THF was added K_2CO_3 (2 M, 25 mL) and the mixture stirred for 10 min. Tetrakis(triphenylphsosphine)palladium(0) (0.50 g, 0.48 mmol) was then added to the reaction mixture and the reaction mixture was heated to reflux for 24 h under a nitrogen atmosphere. The reaction mixture was cooled to room temperature, the solvent was removed under reduced pressure and the product was extracted with ethyl acetate. The organic phase was washed with brine and water and then dried over anhydrous $MgSO_4$. The solvent was removed under reduced pressure and the residue was purified by column chromatography using a mixture of *n*-hexane and EtOAc as eluent to give a yellow solid product (TAAPB) in 68% yield. **^{1}H NMR** (400 MHz, $CDCl_3$): δ 8.18 (d, J = 8.0 Hz, 2 H,), 7.72 (d, J = 8.4 Hz, 2 H), 7.65 (d, J = 8.0 Hz, 2 H), 7.30-7.36 (m, 6 H),

6.93-7.00 (m, 8 H), 2.23 (s, 6 H)); **^{13}C NMR** (100 MHz, $CDCl_3$): δ 145.7, 137.9, 135.9, 133.2, 131.9, 131.4, 130.6, 130.5, 129.9, 127.4, 126.6, 125.8, 124.8, 122.1, 120.2, 20.8.

Synthesis of (4-(9*H*-carbazol-9-yl)phenyl)(phenyl)phosphine oxide (CzPPO)

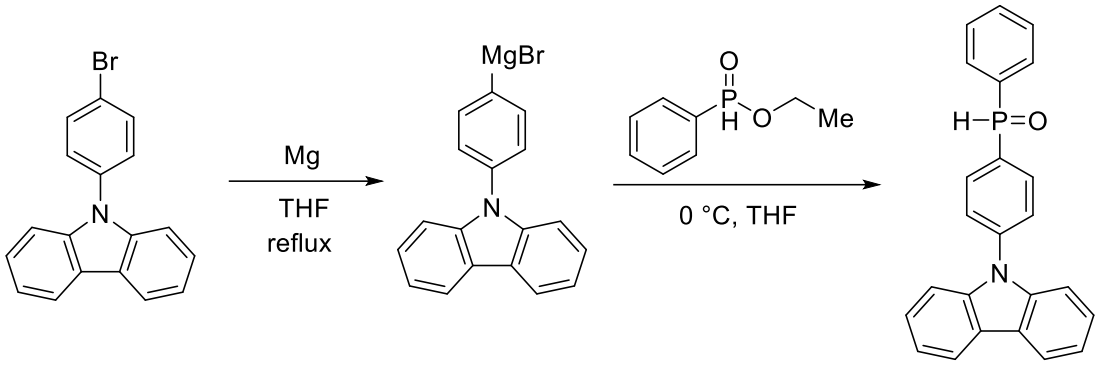

Ethyl phenyl phosphinate (1.1 g, 6.5 mmol) was added dropwise at 0 °C to a solution of 4-carbazole phenyl magnesium bromide in tetrahydrofuran (20 ml), which was prepared from 1-bromo-4-phenyl carbazole (3.0 g, 9.3 mmol) and magnesium (0.899 g, 37.0 mmol). The mixture was aged for 30 minutes at 0 °C, then stirred at ambient temperature for 16 h. The mixture was cooled again to 0 °C, and 75 mL aqueous NH_4Cl was then added slowly. The mixture was extracted with diethyl ether and the organic phase was washed with aqueous $NaHCO_3$ and brine, then it was dried over Na_2SO_4. After the solvent had been completely removed, the residue was used to for next step to synthesize the final compound (CzA-PPO).

Table S1. Crystal data and structure refinement for **TAA-PPO**.

Identification code	TTA-PPO	
Empirical formula	C_{46} H_{36} N O P	
Formula weight	649.73	
Temperature	100(2) K	
Wavelength	0.71073 Å	
Crystal system	Monoclinic	
Space group	C 1 2/c 1	
Unit cell dimensions	a = 36.2541(10) Å	α = 90°.
b = 8.8399(3) Å	β = 100.3730(10)°.	
c = 21.2189(6) Å	γ = 90°.	
Volume	6689.1(3) Å3	

Z	8
Density (calculated)	1.290 Mg/m3
Absorption coefficient	0.121 mm-1
F(000)	2736
Crystal size	0.30 x 0.15 x 0.15 mm3
Theta range for data collection	1.95 to 26.48°.
Index ranges	-45<=h<=45, -11<=k<=6, -26<=l<=26
Reflections collected	25022
Independent reflections	6873 [R(int) = 0.0234]
Completeness to theta = 26.48°	99.3 %
Absorption correction	Semi-empirical from equivalents
Max. and min. transmission	0.9486 and 0.8905
Refinement method	Full-matrix least-squares on F2
Data / restraints / parameters	6873 / 0 / 444
Goodness-of-fit on F2	1.019
Final R indices [I>2sigma(I)]	R1 = 0.0375, wR2 = 0.0905
R indices (all data)	R1 = 0.0474, wR2 = 0.0979
Largest diff. peak and hole	0.408 and -0.381 e.Å-3

DFT Calculations

A time-dependent density functional theory (TDDFT) investigation for TAA-PPO and CzA-PPO were performed using the Gaussian 09 program package in the delta-cluster of SERC facility @IISc. The ground state molecular geometries of these compounds were optimized employing density functional theory (DFT) B3LYP hybrid functional and 6-311G(d,p) basis set in Gaussian 09 Revision A.02 software.[3-5] The TDDFT calculations with the same functionality and the basis set was employed to obtain the excited-state structure. GaussView 5.0 and Chemcraft (version 1.8) were used to analyze the molecular orbitals. The iso values ±0.03 and ±0.001 were used for the HOMO-LUMO orbital picture and hole-electron distributions, respectively. The spatial distributions of the highest occupied molecular orbital (HOMO) and the lowest unoccupied molecular orbital (LUMO) and hole-electron distributions are shown in Fig. 2 and Fig. S1. The singlet and triplet excited states including hole and electron distributions were analysed using *Multiwfn* program package.[6]

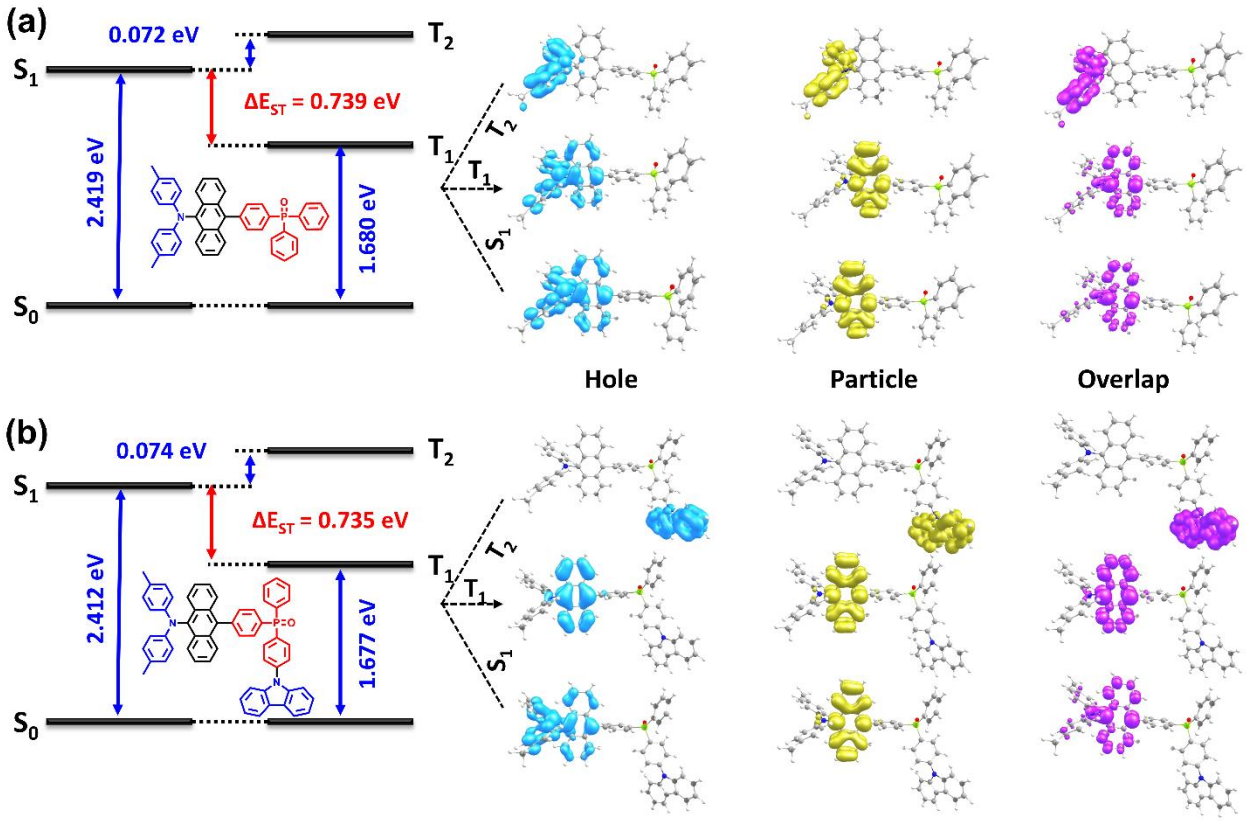

Fig. S1 The TDDFT calculated energy diagram and the hole–electron distributions describing the excitation characters of the S_1, T_1 and T_2 states of (a) TAA-PPO and (b) CzA-PPO are shown. The weights of the hole–electron overlap to the excitations are included. (Isovalue = 0.001)

The holes for S_1 states are located on the donor diphenylamine core and slightly extended to the anthracene π-spacer unit. At the same time, the particles are distributed on anthracene core for both TAA-PPO and CzA-PPO. However, the holes and particles for both the compounds are differently distributed in the T_2 state. The holes and particles are distributed mainly on the diphenylamine core for TAA-PPO in the T_2 state, and it is distributed over the carbazole core for CzA-PPO. This is indicating the LE character of the T_2 excited state for both compounds. The distribution of HOMO-LUMO and the hole/particles suggest that the S_1 and T_1 states are mostly CT characters, and T_2 having LE character observed theoretically.

Additionally, higher singlet-triplet splitting (ΔE_{ST}) was observed for both emitters (Fig. 2, Fig. S1). This is ruling out the possibility for the delayed fluorescence through reverse intersystem crossing (RISC). Therefore, the electrical excitation of these emitters produces a dense triplet

excited-state (75%), leading to triplet-triplet annihilation (TTA).[7-9] As a consequence, delayed emission was observed from the device (G2) originated from the TTA.

Solvatochromism studies: Lippert-Mataga plot

Solvent-dependent shifts in the fluorescence maxima of the molecules can be mainly attributed to the dipole-dipole interactions between the fluorophore and solvent.[10, 11] Positive solvatochromism is observed when there is a redshift in emission with increasing the solvent polarity.[11] This is because of the stabilized excited state. The Lippert-Mataga (L-M) theory describes the solvent dependence spectral shifts as given in Eq. 1.

$$\Delta\nu = \bar{\nu}_a - \bar{\nu}_f = \frac{2}{hc}\left(\frac{\varepsilon - 1}{2\varepsilon + 1} - \frac{n^2 - 1}{2n^2 + 1}\right)\frac{(\mu_E - \mu_G)^2}{a^3} + constant \quad \ldots. \ (1)$$

Where: $\bar{\nu}_a = \frac{1}{\lambda_{abs}^{max}}$, $\bar{\nu}_f = \frac{1}{\lambda_{em}^{max}}$ $and\ \Delta f = \left(\frac{\varepsilon-1}{2\varepsilon+1} - \frac{n^2-1}{2n^2+1}\right)$ …. (2)

In this theory, specific solvent-fluorophore interactions, such as hydrogen bonding are not included. Eq. 1 shows Stokes shift ($\Delta\bar{\nu}$) depends on the dipole moments of the fluorophore in the ground (μ_G) and the excited (μ_E) state, respectively. It also depends on the dielectric constant (ε) and the refractive index (η) of the corresponding solvent. $\bar{\nu}_a$ and $\bar{\nu}_f$ represent the wavenumbers of the absorption and the fluorescence emission, respectively, *h* is the Planck's constant, *c* is the speed of light in vacuum, and *a* is the Onsager radius of the cavity in which the fluorophore resides. Δf is the orientation polarizability of the solvent (Eq. 2). Plotting the Stokes shift as a function of the orientation polarizability of the solvents gives the Lippert-Mataga plot (Fig. S2).

Table S2 Reichardt's solvent polarity parameters $E_T(30)$/ E_T^N, dielectric constants (ε), refractive indices (η), orientation polarizabilities (Δf) of different solvents including the Stokes shift ($\Delta\bar{\nu}$) of (a) TAA-PPO and (b) CzA-PPO as a function of the different solvents.

Solvent parameters						TAA-PPO		CzA-PPO		Stokes shift $\Delta\bar{\nu}$ (cm^{-1})	
Entry	**$E_T(30)$ [kcal mol^{-1}]**	**E_T^N**	**ε**	**η**	**Δf**	**λ_{abs}**	**λ_{em}**	**λ_{abs}**	**λ_{em}**	**TAA-PPO**	**CzA-PPO**
n-hexane	31	0.009	1.88	1.375	0.0012	448	490	452	490	1913	1715
Toluene	33.9	0.099	2.38	1.497	0.013	452	520	452	522	2893	2966
THF	37.4	0.207	7.58	1.407	0.210	446	536	446	537	3765	3800
DCM	40.7	0.309	8.93	1.424	0.217	446	550	446	550	4240	4240

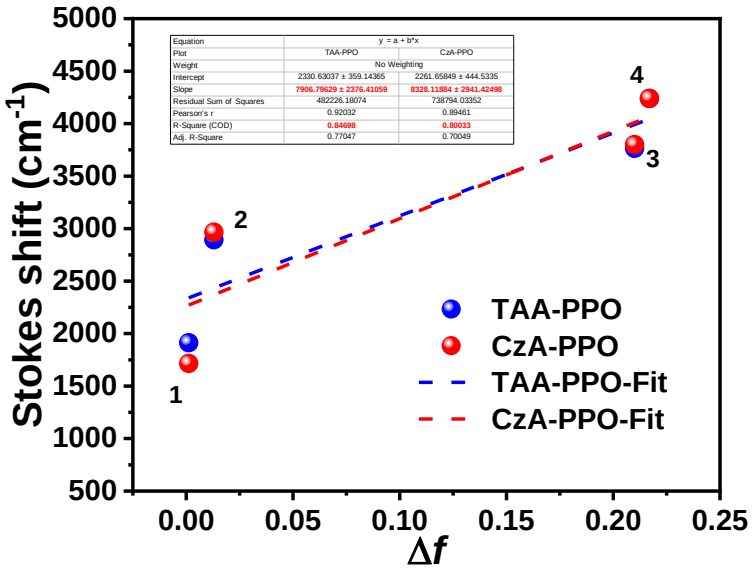

Fig. S2 Lippert-Mataga plot depicting Stokes shift ($\Delta\bar{\nu}$)versus the solvent orientation polarizability (Δf) of (a) TAA-PPO and (b) CzA-PPO. The numbers refer to the solvents: (1) n-hexane (2) toluene, (3) tetrahydrofuran, and (4) dichloromethane. The dashed line represents the best linear fit to the data points.

The change of the dipole moment (Δμ) can be estimated using the equation (1) from the slope obtained from the L-M plot as following

$$(\mu_E - \mu_G)^2 \;=\; \frac{Slope * (\mathrm{h}ca^3)}{2} \ldots. \; (3)$$

$\Delta\,\mu(\mu_E - \mu_G)$ is the change of dipole moment from the ground to an excited state.

Table S3 Fitting parameters of Lippert-Mataga plots and calculated Onsager radius (a), $\Delta\mu$ ($\mu_E - \mu_G$) refers the change in dipole moment. (R^2: goodness of fit)

Compound	Slope (cm^{-1})	Intercept (cm^{-1})	R^2	a (Å)*	($\mu_E - \mu_G$) D
TAA-PPO	7906	2330	84.7	4.28	7.8
CzA-PPO	8328	2261	80.0	4.70	9.3

*The Onsager radius can be calculated from the geometry optimized structure of the compounds using DFT minimization in Gaussian program (B3LYP functional using 6-31G-(d) orbital base).

The experimental value of the transient dipole moment ($\Delta\mu$) obtained from the L-M plot for TAA-PPO and CzA-PPO are 7.8 and 9.3 D, respectively (Fig. S2, Table S2-S3). We estimated the ground-state dipole (μg) for both the compounds using long-range correction density-functional-theory (DFT) calculation by the Gaussian 09 package at CAM-B3LYP/6-311G(d,p) level.[12] The polarizable continuum model (PCM) was employed in nonpolar toluene and polar DCM media for both the compounds. The positive solvatochromism and prominent change of transient dipole moment ($\Delta\mu$) values confirm the charge transfer (CT) behavior of the molecules.[11]

The calculated values of ground state dipole moment (μ_G) are 5.13 and 6.05 D for TAA-PPO in toluene and DCM, respectively. Therefore, the value of excited-state dipole moment (μ_E) of TAA-PPO in toluene is 12.93 D, and 13.85 D in DCM was estimated. Similarly, the excited state dipole moment (μ_E) 14.2 D (μ_G = 4.91 D) and 15.03 D (μ_G = 5.73 D) was estimated for CzA-PPO in toluene and DCM, respectively. The large excited-state dipole moment in non-polar as well as polar medium indicates the CT nature in both the medium. [12, 13] Additionally, we observed a single emission peak in the non-polar and polar medium due to CT-emission, and no LE peaks were observed for both the compounds.

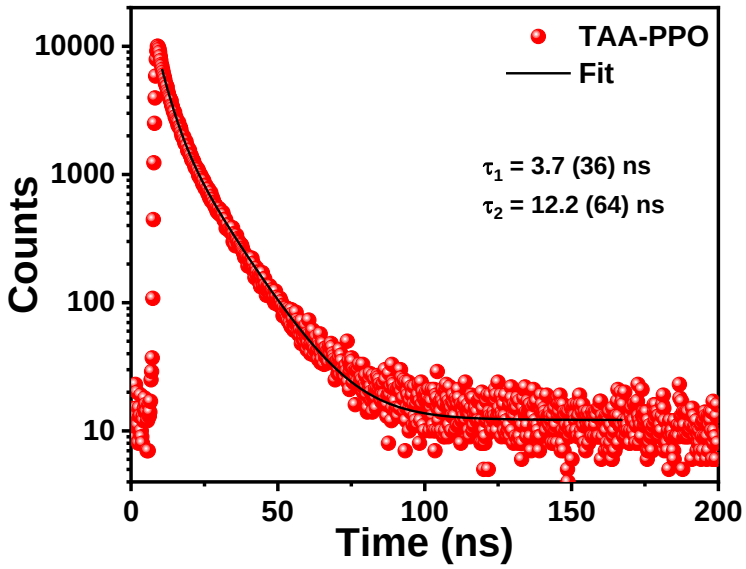

Fig. S3 Transient decay profile of TAA-PPO (λ_{ex} = 450 nm, λ_{ex} = 525 nm) neat film at room temperature.

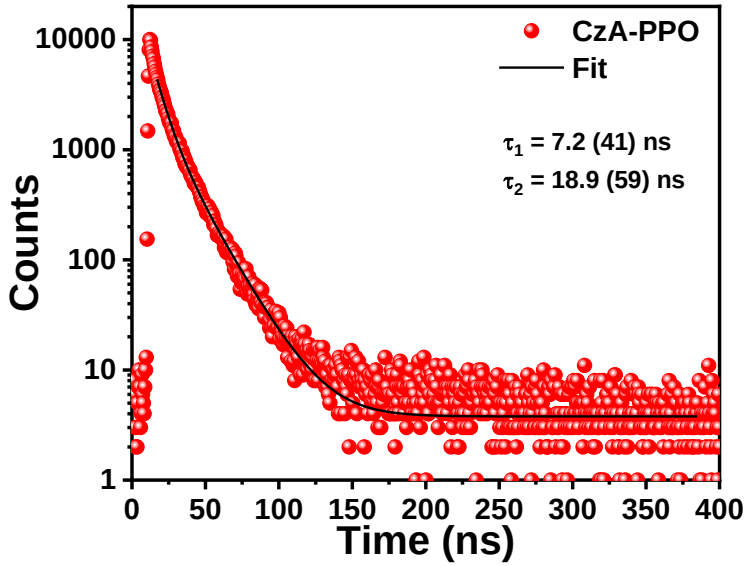

Fig. S4 Transient decay profile of CzA-PPO (λ_{ex} = 450 nm, λ_{ex} = 540) nm neat film at room temperature.

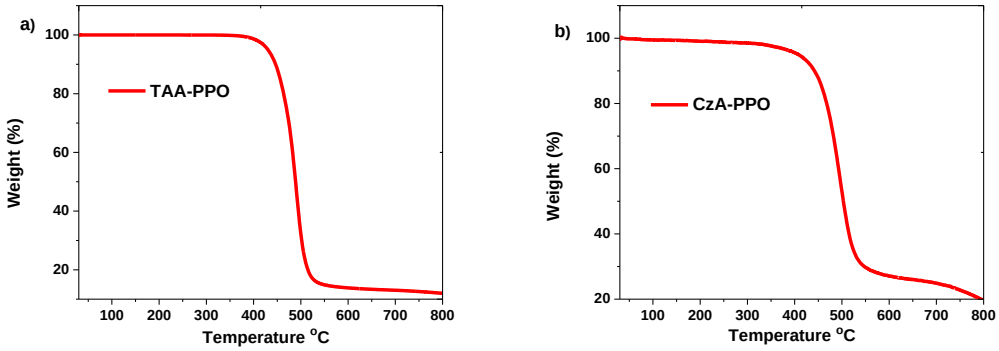

Fig. S5 The thermograms of a) TAA-PPO and b) CzA-PPO.

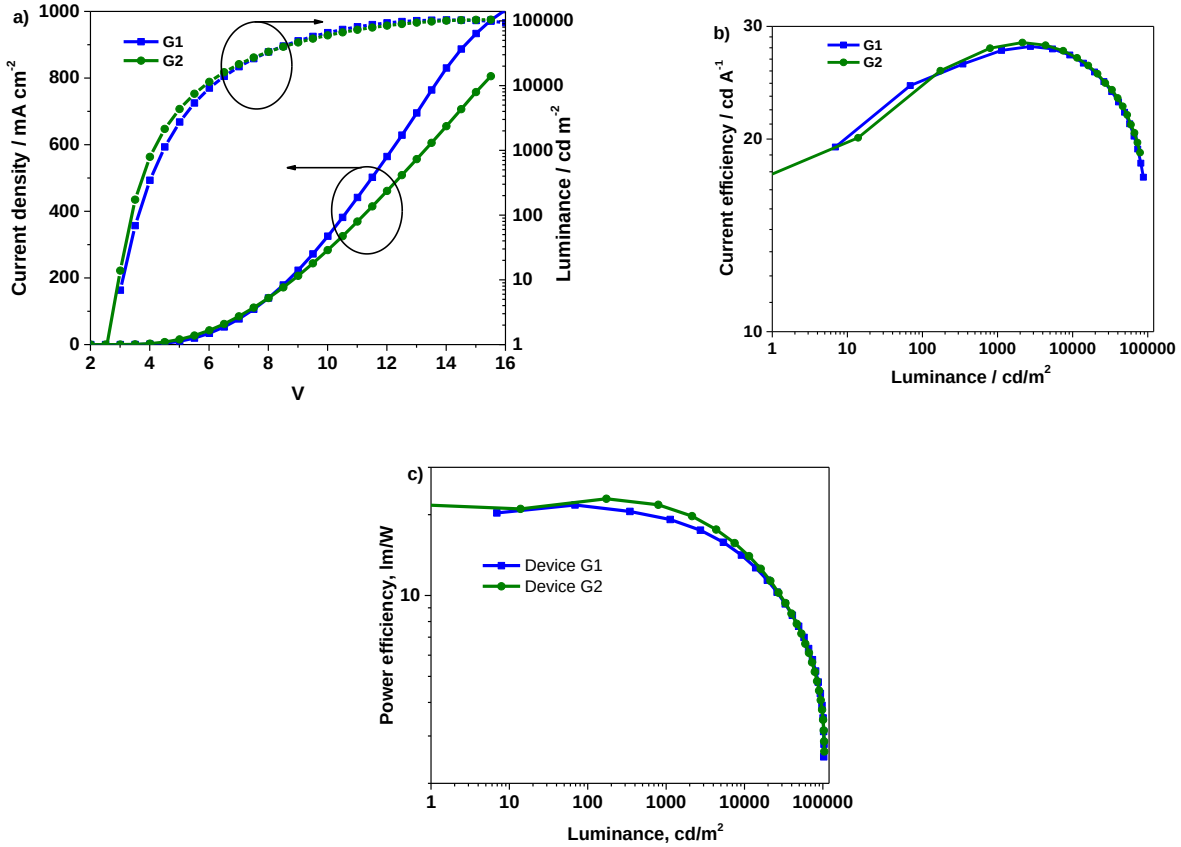

Fig. S6 a) current density and luminance vs driving voltage; b) current efficiency vs luminance; c) The power efficiency vs luminance of devices G1 and G2.

Table S4. Current efficiency (CE) of the device G1 and G2 at different luminance values.

Device	Emitter	CE [100 cd/m^2]	CE [500 cd/m^2]	CE [1000 cd/m^2]	CE [5000 cd/m^2]	CE [10000 cd/m^2]	CE [20000 cd/m^2]
G1	TAA-PPO	24.7	26.4	27.3	27.7	27.0	25.4
G2	CzA-PPO	24.2	26.9	27.9	27.9	27.0	25.4

CE - current efficiency

Table S5. EQE of the device G1 and G2 at different luminance values.

Device	Emitter	EQE / % [100 cd m^{-2}]	EQE / % [500 cd m^{-2}]	EQE / % [1000 cd m^{-2}]	EQE / % [5000 cd m^{-2}]	EQE / % [10000 cd m^{-2}]	EQE / % [20000 cd m^{-2}]
G1	**TAA-PPO**	6.1	6.7	6.9	7.1	6.8	6.5
G2	**CzA-PPO**	6.1	6.9	7.1	7.1	6.9	6.5

EQE = external quantum efficiency

Table S6. EL performances of the device with a TADF assistant dopant[a]

Device	Emitter	V_d[b] / V	L_{max} / cd m^{-2}	EQE$_{max}$ / %	CE$_{max}$ / cd A^{-1}	PE$_{max}$ / lm W^{-1}	λ_{EL} / nm at 8V	CIE at 8V / (x, y)
G3	TAA-PPO	3.5	33149 (15.0)	17.8 (4.0)	61.6 (4.0)	48.1 (4.0)	518	0.23, 0.58

[a]Device configuration: ITO/HAT-CN (10 nm) /TAPC (20 nm) /*m*CBP: 4BPy-*m*DTC (7 wt%):TAA-PPO (1 wt%) (20 nm) /TmPyPB (55 nm) /LiF (1 nm)/ Al,). CE$_{max}$= maximum current efficiency. PE$_{max}$ = maximum power efficiency. λ_{EL} = the wavelength where the EL spectrum has the maximum intensity. Value in parentheses are at 500 cd m^{-2}. [b]V_d, the operating voltage at a brightness of 1 cd/m^2

Hyperfluorescence analysis: Förster Resonance Energy Transfer (FRET)

We have demonstrated the hyperfluorescence devices based on the TTA-PPO compound coupled with the TADF dopant 4BPy-*m*DTC.[14] The extensive time-resolved spectroscopic measurements were carried out to establish the Förster resonance energy transfer (FRET) process.[15-17] The Förster resonance energy transfer (FRET) from S_1 of TADF emitter (4BPy-*m*DTC) to S_1 of TTA-PPO occurred because the absorption spectrum of TTA-PPO is considerably overlapped with the emission spectrum edge of 4BPy-*m*DTC (Fig. 8a).[17]

The steady-state emission measurements of spin-coated films of TAA-PPO and 4BPy-*m*DTC with mCP host at room temperature also indicate the FRET process (Fig. S7). The emission spectrum of 4BPy-*m*DTC film spin-coated with mCP host exhibits the peak maxima at λ_{em} = 490 nm (λ_{ex} = 350 nm). However, the emission of 4BPy-*m*DTC in the presence of TAA-PPO shifted to 525 nm while exciting at λ_{ex} = 350 nm. This is exactly the emission of TAA-PPO neat film with mCP host at λ_{ex} = 450 nm. Therefore, the energy transfer from the 4BPy-*m*DTC to TAA-PPO is occurring, resulting in the emission from TAA-PPO only while exciting at 4BPy-*m*DTC excitation.

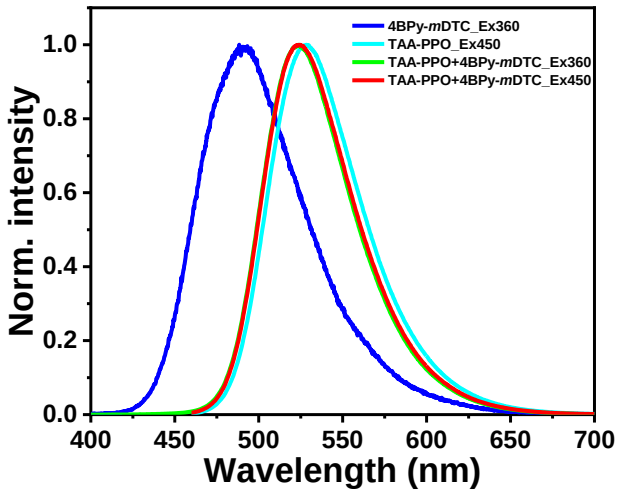

Fig. S7 Normalized emission spectra of 4BPy-*m*DTC (λ_{ex} = 350 nm) and TAA-PPO (λ_{ex} = 450 nm) films drop casted using mCP host at room temperature.

The long-lived emission decays of TTA-PPO and TADF dopant (4BPy-*m*DTC) films with mCP host were recorded (Fig. 8b, main text). No significant long-lived species was found for the TTA-PPO spin-coated film with mCP host at room temperature, indicating no TADF characteristic. The prominent long-lived species with biexponential decay were observed for 4BPy-*m*DTC film with

mCP host. This is due to the delayed fluorescence of 4BPy-*m*DTC.[14] A similar biexponential decay was found while exciting at 4BPy-*m*DTC's excitation maxima (λ_{ex} = 350 nm) and collecting emission at 4BPy-*m*DTC's emission (λ_{em} = 490 nm) for the 4BPy-*m*DTC+TAA-PPO spin-coated film with mCP host. However, triexponential decay was observed while collecting the emission at TAA-PPO maxima (λ_{em} = 525 nm). Fig. 8b and Table S7 clearly shows that there is a reduction in the lifetime of 4BPy-*m*DTC in the presence of TAA-PPO and confirms the efficient energy transfer from 4BPy-*m*DTC to TAA-PPO.

Table S7. Emission decay parameters (λ_{ex}= 350) for 4BPy-*m*DTC and TAA+4BPy-*m*DTC films drop-casted using mCP host at room temperature; the decay times (τ_1, and τ_2), the respective fractional contributions (α_1, and α_2 mentioned in parentheses), the weighted average decay time ($\tau_{avg.}$) and the quality of fitting ($\chi 2$) are shown.

Sample	λ_{ex} (nm)	λ_{em} (nm)	τ_1 (μs)	τ_2 (μs)	$\tau_{avg.}$ (μs)
mCP+4BPy-*m*DTC	350	490	24.9 (39)	60.9 (61)	46.86
mCP+4BPy-*m*DTC+TAA	350	490	13.4 (52)	51.5 (48)	31.68

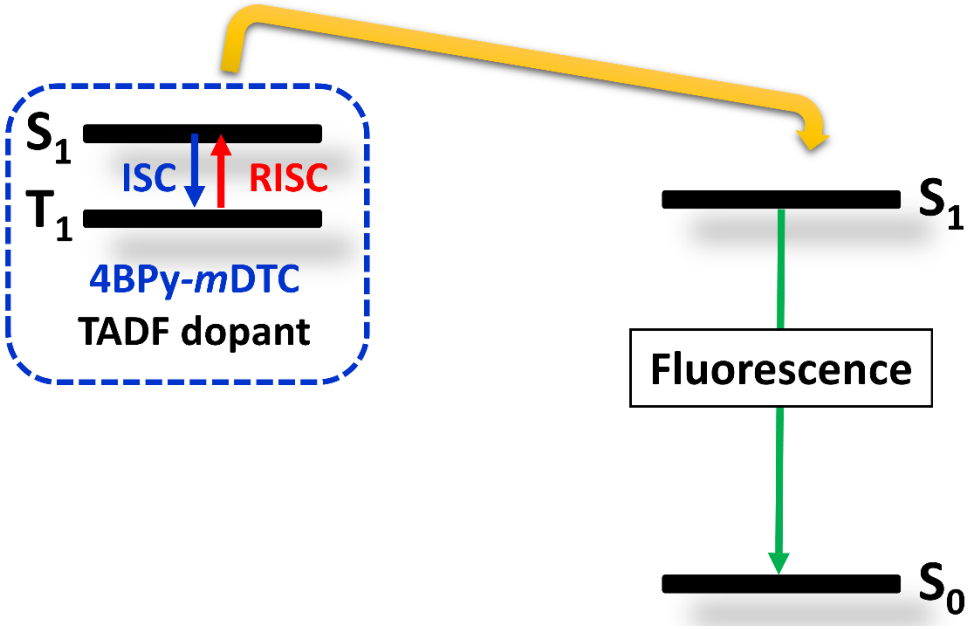

Scheme S1. Schematic illustration of plausible energy transfer pathways for the hyperfluorescence devices.

References

1. J.-J. Lin, W.-S. Liao, H.-J. Huang, F.-I. Wu and C.-H. Cheng, *Adv. Funct. Mater.*, 2008, **18**, 485-491.
2. P. Rajamalli, P. Gandeepan, M.-J. Huang and C.-H. Cheng, *J. Mater. Chem. C*, 2015, **3**, 3329-3335.
3. C. Lee, W. Yang and R. G. Parr, *Phys. Rev. B*, 1988, **37**, 785-789.
4. B. Miehlich, A. Savin, H. Stoll and H. Preuss, *Chem. Phys. Lett.*, 1989, **157**, 200-206.
5. A. D. Becke, *J. Chem. Phys.*, 1993, **98**, 5648-5652.
6. T. Lu and F. Chen, *J. Comp. Chem.*, 2012, **33**, 580-592.
7. C.-J. Chiang, A. Kimyonok, M. K. Etherington, G. C. Griffiths, V. Jankus, F. Turksoy and A. P. Monkman, *Adv. Funct. Mater.*, 2013, **23**, 739-746.
8. M. Aydemir, G. Haykır, A. Battal, V. Jankus, S. K. Sugunan, F. B. Dias, H. Al-Attar, F. Türksoy, M. Tavaslı and A. P. Monkman, *Org. Electron.*, 2016, **30**, 149-157.
9. Y. H. Chen, C. C. Lin, M. J. Huang, K. Hung, Y. C. Wu, W. C. Lin, R. W. Chen-Cheng, H. W. Lin and C. H. Cheng, *Chem. Sci.*, 2016, **7**, 4044-4051.
10. C. Reichardt, *Chem. Rev.*, 1994, **94**, 2319-2358.
11. J. R. Lakowicz, *Principles of fluorescence spectroscopy*, Springer, New York, 2006.
12. W. Li, D. Liu, F. Shen, D. Ma, Z. Wang, T. Feng, Y. Xu, B. Yang and Y. Ma, *Adv. Funct. Mater.*, 2012, **22**, 2797-2803.
13. B. Sk, S. Khodia and A. Patra, *Chem. Commun.*, 2018, **54**, 1786-1789.
14. P. Rajamalli, V. Thangaraji, N. Senthilkumar, C.-C. Ren-Wu, H.-W. Lin and C.-H. Cheng, *J. Mater. Chem. C*, 2017, **5**, 2919-2926.
15. P. Pallavi, B. Sk, P. Ahir and A. Patra, *Chem. Eur. J.*, 2018, **24**, 1151-1158.
16. H. Abroshan, V. Coropceanu and J.-L. Brédas, *ACS Mater. Lett.*, 2020, **2**, 1412-1418.
17. C.-Y. Chan, M. Tanaka, Y.-T. Lee, Y.-W. Wong, H. Nakanotani, T. Hatakeyama and C. Adachi, *Nat. Photonics*, 2021, **15**, 203-207.